Research Article Vol. 30, No. 10 / 9 May 2022 / Optics Express 17371
Optics EXPRESS

Free-standing plasmonic nanoarrays for leaky optical waveguiding and sensing

GIACOMO MANZATO,[1] MARIA CATERINA GIORDANO,[1] MATTEO BARELLI,[1,2] DEBASREE CHOWDHURY,[1] MARCO CENTINI,[3,4] AND FRANCESCO BUATIER DE MONGEOT[1,5]

[1]*Dipartimento di Fisica, Università di Genova, Via Dodecaneso 33, 16146 Genova, Italy*
[2]*Present address: Photonic Nanomaterials Lab, Istituto Italiano di Tecnologia (IIT), 16163 Genova, Italy*
[3]*Dipartimento di Scienze di Base ed Applicate per l'Ingegneria, Sapienza Università di Roma, Via Antonio Scarpa 16, 00161 Rome, Italy*
[4]*marco.centini@uniroma1.it*
[5]*buatier@fisica.unige.it*

Abstract: Flat optics nanogratings supported on thin free-standing membranes offer the opportunity to combine narrowband waveguided modes and Rayleigh anomalies for sensitive and tunable biosensing. At the surface of high-refractive index Si_3N_4 membranes we engineered lithographic nanogratings based on plasmonic nanostripes, demonstrating the excitation of sharp waveguided modes and lattice resonances. We achieved fine tuning of these optical modes over a broadband Visible and Near-Infrared spectrum, in full agreement with numerical calculations. This possibility allowed us to select sharp waveguided modes supporting strong near-field amplification, extending for hundreds of nanometres out of the grating and enabling versatile biosensing applications. We demonstrate the potential of this flat-optics platform by devising a proof-of-concept nanofluidic refractive index sensor exploiting the long-range waveguided mode operating at the sub-picoliter scale. This free-standing device configuration, that could be further engineered at the nanoscale, highlights the strong potential of flat-optics nanoarrays in optofluidics and nanofluidic biosensing.

1. Introduction

Flat-optics nanoarrays have recently gathered strong attention in different fields ranging from nanophotonics [1–5] to nanofluidics [6–8], optical spectroscopies and sensing [9–15]. In this context free-standing nanoarrays [16–18] are particularly attractive due to their capability to host photonic modes within functionalized channels promoting nanofluidic transport [19] and high-resolution biosensing functionalities [20]. Thanks to this peculiar configuration, liquid transport at the nanoscale can be investigated as well as optofluidic effects and label-free biosensing of low-concentration molecule essays [7,16,17]. In this context, the capability to engineer photonic arrays at the surface of thin free-standing membranes, which are transparent over a broadband optical window, is crucial in view of versatile biosensing applications that could span from the Visible to the relevant Near- and Mid-Infrared spectral range [21].

Various sensing templates and configurations have been so far proposed, demonstrating high sensitivity at the surface of thick solid-state substrates thanks to the strong near-field confinement supported by plasmonic nanoantennas and/or thin films [22–28]. However, the state-of-the-art sensors based on thin metallic films require bulky optical setups in Kretschman configuration to launch Surface Plasmon Polaritons at the sample interface [29], thus demanding more compact schemes in view of sensor miniaturization and integration within ultra-thin supports. A promising alternative is based on plasmonic nanoantenna arrays which are characterized by resonant 'hot-spots' localized in the inter-antennas nanogaps [30,31]. By exploiting this effect, a strong enhancement of weak spectroscopic signals can be achieved. In parallel, spectral

#453135 https://doi.org/10.1364/OE.453135
Journal © 2022 Received 12 Jan 2022; revised 22 Mar 2022; accepted 22 Mar 2022; published 5 May 2022

Optics EXPRESS

sensitivity in applications such as refractive index sensing is limited due to the broadband nature of the plasmonic resonance. In order to overcome this limit, plasmonic nanoantennas can be arranged in the form of periodic nanogratings: narrowband Rayleigh Anomalies (RA) can be here excited thanks to the coupling of light momentum to the periodic lattice, thus achieving strong electromagnetic confinement at the plasmonic-dielectric interface. Eventually, tailoring the substrate materials and/or thickness, splitting into two diffraction modes can be observed supported at the substrate-metal and at the metal-air interface, respectively. Under this condition two different effects can be engineered by properly tailoring the nanopatterning conditions: (i) resonant coupling of the RA to the broadband plasmon mode, resulting into narrowband Lattice Resonances due to Fano interference [32,33]; (ii) guiding and/or waveguiding of the leaky propagating mode within the substrate. Improved spectral sensitivity can be achieved in the first case thanks to sharp Fano resonances [34–36], while substrate-guiding mechanisms such as Guided Mode Anomalies (GMA) represent a very effective way to amplify light coupling to the metasurface, promoting high sensitivity in Raman spectroscopy [37], or strong photon absorption enhancement in ultrathin two-dimensional (2D) layers [38–40].

When high refractive index substrates are employed, more efficient light-guiding can be achieved and gratings can promote resonant electromagnetic confinement into the waveguide. Different schemes have been investigated so far, based both on plasmonic [41] and/or dielectric gratings [42], for launching and coupling leaky waveguided modes which can be tuned across a broadband spectral range by acting on the metasurface materials and design. Both all-dielectric and hybrid plasmonic/dielectric Guided Mode Resonant (GMR) gratings have been proposed and optimized for a broad range of applications, from diffractive elements to biosensors thanks to the huge variety of available materials and tuning capability [43]. In particular, a hybrid scheme supporting both photonic and plasmonic modes has been recently proposed for large biomolecules sensing [44]. Concerning GMR gratings realized on freestanding membranes, asymmetric light absorbers/reflectors to be implemented in energy harvesting applications and for wavelength multiplexing [45,46] have been designed and fabricated on Si_3N_4 slabs coupled to metallic nanostructures.

Thin and free-standing supports endowed with high refractive index represent a unique platform where flat-optics gratings can combine effective waveguiding to near field confinement at the interface, with crucial impact in optofluidics and biosensing. Indeed, the possibility to design optically active nanofluidic channels is intriguing since, on one side opens the possibility to study interaction between light and fluid transport [19,47], and on the other side enables the design of compact free-standing nanosensors [6,48].

In this work we engineered plasmonic nanogratings supported on high-refractive index, free standing membranes by high resolution nanolithography. A flat-optics nanograting based on Au nanostripes is fabricated at the surface of thin Si_3N_4 membranes, thus enabling the excitation of narrowband Rayleigh Anomalies and waveguided modes, coupled to the localized plasmon resonance characteristic of the nanoantenna elements. Thanks to the versatile flat-optics platform, accurate tuning of the optical modes has been achieved over a broadband Visible and Near-IR spectrum, obtaining an optimal agreement with respect to calculations. The accurate modeling of the system also enables engineering of the optical configuration for which narrowband waveguided modes induce a strong near-field confinement at the external interface, potentially acting as hot-spots for sensing. The performances of these flat-optics templates have been finally tested into a proof-of-concept nanofluidic device, showing good figures of merit in refractive index sensing. The highest figures of merit reported in literature are usually obtained in specialized configurations, adopting illumination at tilted incidence angles which are not accessible under the high numerical aperture microscope objectives of a typical setup. The proposed nanofabricated platform is peculiar since it makes possible measurements on miniaturized plasmonic arrays employing a conventional low-cost optical setup under normal incidence illumination conditions.

Optics EXPRESS

2. Results and discussion

Periodic plasmonic nanostripe arrays are fabricated on top of electron-transparent silicon nitride (Si_3N_4) membranes via high resolution electron beam lithography (EBL), achieving homogeneous patterned area extending over hundreds of square microns (Fig. 1(a), 1(b). Thanks to their compatibility with nanofluidic sensing we choose free standing Si_3N_4 membranes (Agar Scientific - thickness 200 nm). The free-standing square membrane (~ mm^2) is supported by a silicon chip as shown in Figure 1(a) (see Fig. S1 in Supplement 1 for further details).

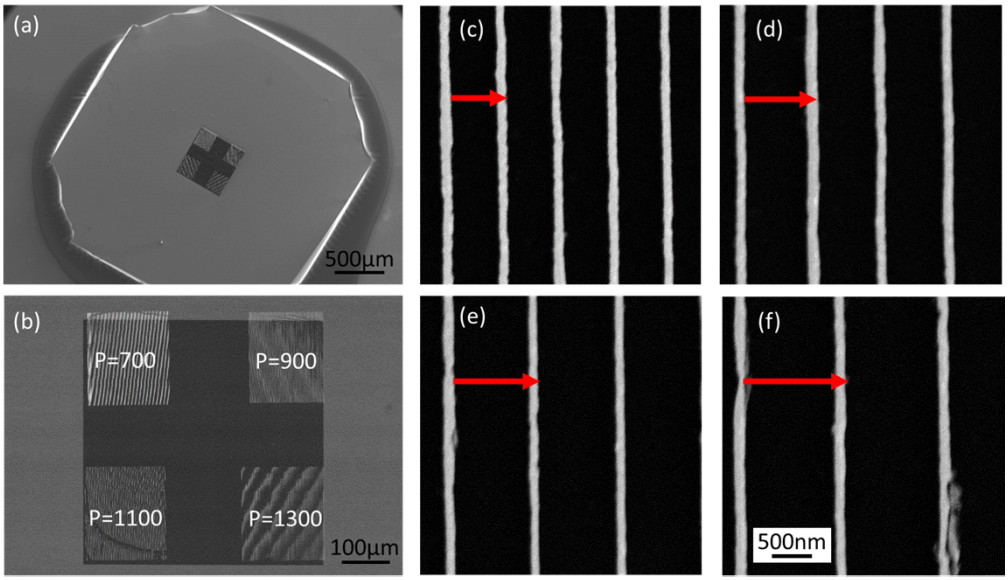

Fig. 1. SEM images of the studied sample. (a) Low magnification image of the 3 mm chip, with the square free-standing window visible in the middle; (b) detail of the free-standing area: four patterns with marked period have been fabricated without overlap. The apparent distortion of the patterns is simply a graphical artifact due to Moiré effect; (c-f) images of the nanostripes arrays with period respectively 700, 900, 1100 and 1300 nm. Magnification of the SEM images is the same (scale bar 500 nm).

The Scanning Electron Microscope (SEM) image of Fig. 1(b) well highlights the presence of four patterns on the same substrate, which are characterized by different periodicity of the lattice, P, ranging from 700 nm to 1300 nm, thus enabling the fine tuning of the optical response of these free-standing gratings. SEM images shown in Fig. 1(c) and Fig. 1(f), respectively corresponding to increasing periodicity of the pattern from $P = 700$ nm to $P = 1300$ nm, highlight the degree of order of the nanopatterns and the control on the periodicity and shape of the antennas. All the patterns are based on nanostripes characterized by fixed aspect ratio, determined by width $w = 120$ nm and thickness $h = 40$ nm, engineered with the aim to tune the optical modes within the Visible (VIS) and Near-Infrared (NIR) spectrum.

The optical response of these arrays has been investigated via optical micro-spectroscopy, using a custom modified optical microscope (Labomed), operating in transmission configuration (Fig. 2(a) and fibre-coupled to a VIS-NIR spectrometer (Ocean Optics). A white light beam is shone from a halogen lamp through a polarizer and a condenser lens, finally illuminating the bottom surface of the sample at normal incidence (Fig. 2(a). A 100x magnification objective collects the optical intensity transmitted from a micro-spot (diameter ~20 µm).

Due to the order of these periodic arrays and to the subwavelength size of the Au nanostripes, different optical modes are expected to occur in the VIS and NIR spectral ranges. Indeed, the

Optics EXPRESS

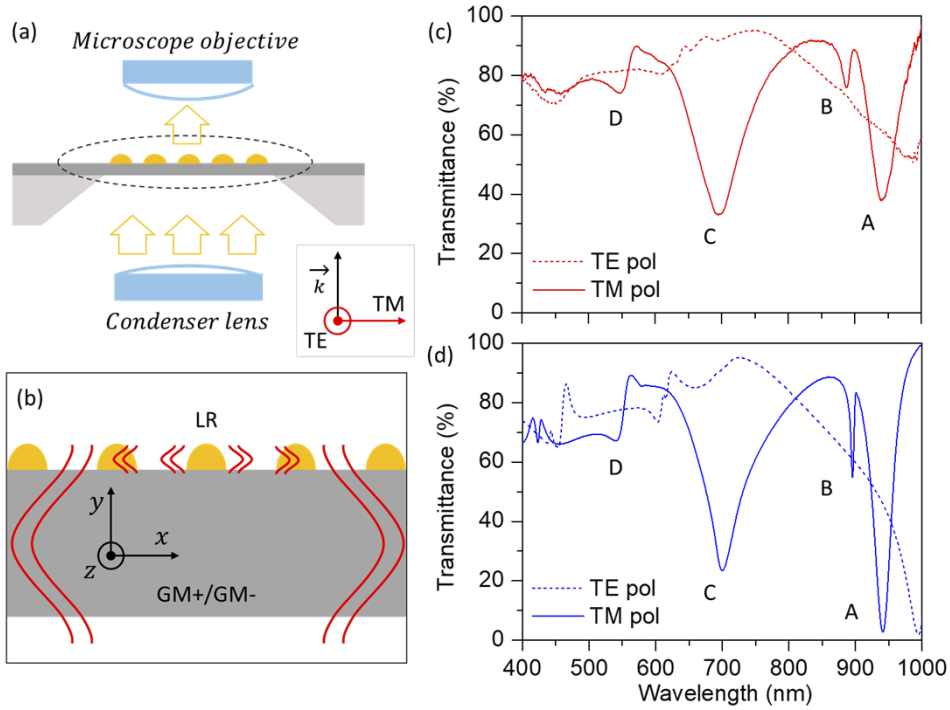

Fig. 2. (a) Schematic representation of the optical setup, based on an optical microscope fiber-coupled with a spectrometer; (b) sketch of the photonic modes sustained by the nanoarrays: the plasmonic nanostripe gratings behave as plasmonic antennas supporting lattice resonances (LR) and launching guided modes in the high index substrate (GM+, GM-); (c,d) Experimental and simulated optical response of the P700 array, respectively. The transmission microspectra were measured and calculated by sample excitation with polarized light, both perpendicular (TM- solid curves) and parallel (TE -dashed curves) to the nanostripes long axis.

Au nanostripes behave as plasmonic nanoantennas and, at the same time, the periodic grating may support Rayleigh Anomalies (RA). Under this condition the so-called Lattice Resonances (LR) confined at the surface (see sketch in Fig. 2(b) can be observed due to resonant interference between RA and plasmonic mode [49]. Additionally, guided modes (GM+/GM-) can be launched into the high index substrate, due to resonant interaction with the periodic nanograting (see sketch in Fig. 2(b).

In Fig. 2(c) the normal incidence transmission microspectra of the pattern P700 are shown, corresponding to two perpendicular polarizations of the excitation beam. The light is polarized either parallel (TE-pol, dashed curves) or perpendicular (TM-pol, solid curves) to the long axis of the nanostripes. A strong optical dichroism is detected in these anisotropic arrays. For TE polarization, a slight decrease of transmittance is observed for wavelength below 500 nm, due to inter-band transitions in gold, in resonance with high order optical modes. Additional weak modes are observed at higher wavelength. For TM polarization, we detect high-energy optical modes ($\lambda \sim$ 400-450 nm) that can be associated to the presence of the Si_3N_4 waveguide beneath the pattern, and to the generation of multiple guided modes [50]. At higher wavelengths, four sharp modes are detected within the VIS and NIR spectrum, above the Au interband transition. The first minimum is visible at 540 nm (mode D in Fig. 2(c), a broader lattice resonance is detected at 700 nm and marked as mode C. Given the geometrical aspect ratio of the nanostripes, we indeed expect a

Optics EXPRESS

localized plasmon resonance within this spectral range. Single stripe extinction cross-section calculations (see Fig. S2 in Supplement 1) show a broadband plasmonic resonance excited at about 750 nm wavelength. This feature provides a good coupling efficiency between the grating and the photonics guided modes leading to possible plasmonic/photonic mode hybridization over a broad wavelength range. Two further narrowband minima are visible in the NIR spectrum (mode B at 900 nm, mode A at 940 nm) corresponding to the first order guided modes. Experimental spectra have been confirmed by finite-difference time-domain (FDTD) calculations of finite structures (removing periodic boundary conditions), considering an incident Gaussian field of 10 μm beam waist. Numerical results depicted in Fig. 2(d) are in remarkable agreement with the experimental data (Fig. 2(c). Due to the symmetry of the system, using finite size spots fulfilling normally incident plane wave approximation, one would expect the resonant excitation of left to right (LTR) or right to left (RTL) guided modes that are degenerate in frequency. Conversely, in our system we observe a peculiar double peak behaviour (modes A, B and modes C, D) that can be attributed to the transverse components of the wavevector with respect to the surface normal. Indeed, a plane wave expansion of a real focused beam contains also wavevectors components corresponding to nonzero incidence angles (θ). These components can couple to the guided modes according to the following equation:

$$\frac{2\pi}{\lambda} sin(\theta) + \frac{2\pi}{\Lambda} m = \pm \frac{2\pi}{\lambda} n_{eff} \tag{1}$$

where λ is the wavelength, Λ is the periodicity of the grating, the integer m is the diffraction order of the grating and the sign + (-) stands for the same (opposite) direction of propagation of the guided mode (of effective refractive index neff) with respect to the incident light. The (+) and (-) solutions of Eq. (1) respectively correspond to modes such as A (GM+) and B (GM-), and to all the higher order pairs.

Since, for a symmetric normal incident Gaussian beam the amount of LTR and RTL coupled energy is the same we are not able to distinguish the two contributions. To validate our hypothesis about the nature of the peaks, in the first place, simulations are conducted focusing the attention on the field distribution of the four labelled modes. In the case of the lattice resonance, we expect the electromagnetic field to be confined at the nanoantenna's surface, while for pure guided modes we expect the typical single layer symmetric waveguide field distributions [51–53]. In Fig. 3 we observe the spatial distribution of both magnetic (H/H0 - first two columns on the left) and electric (E/E0 - right columns) field. The system supports a combination of different leaky waveguide modes with symmetric optical field distribution perpendicularly to the guide (y axis). The calculated distribution of the magnetic field of mode A, B and D (Fig. 3(a), 3(e), 3(m)) suggests a symmetric behaviour. Conversely, in the case of mode C, calculations show an asymmetric magnetic field distribution (Fig. 3(i), with strong localization in proximity of the nanoantenna grating attributed to the resonant interference with the broader lattice resonance supported by plasmonic nanoantennas.

Additionally, strong interference fringes are observed along the waveguide (x axis), arising from the superposition of LTR and RTL counter-propagating guided modes. While A, B and D (Fig. 3(a), 3(e), 3(m) are based on the unperturbed fundamental TM0 guided mode of the Si_3N_4 slab, mode C (Fig. 3(i) displays the typical central node of the TM1 mode.

A deeper analysis of the zoomed magnetic and electric field distributions across the slab section reveals high symmetry for modes B (Fig. 3(f), 3(g) and D (Fig. 3(n), 3(o), typical of dielectric waveguided modes. On the other hand, in the case of mode A (Fig. 3(a), 3(b) and C (Fig. 3(i), 3(j) the optical field distributions are asymmetric and mainly confined on the grating side. In particular mode C with plasmonic character shows an electric field strongly confined within a few nanometres at the surface (Fig. 3(k), while mode A shows broader distribution out of the substrate (Fig. 3(c). It is worth noticing that all the waveguided modes detuned with respect to the lattice resonance are characterized by electric field (Ey/E0) strongly amplified

Optics EXPRESS

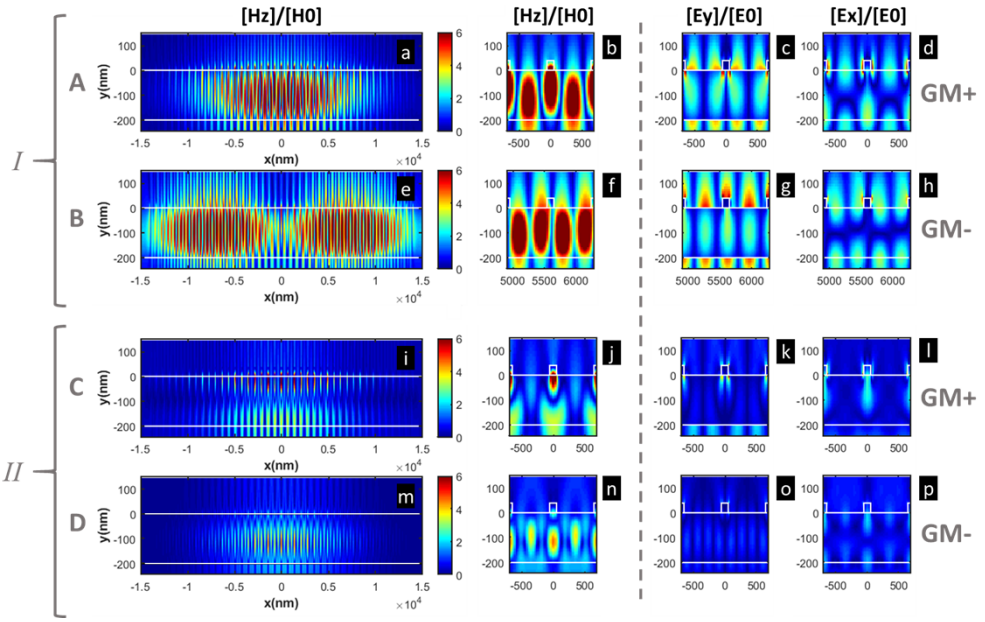

Fig. 3. Calculated field maps of the four detected modes, represented along the cross section of the membrane with the nanostripes on the upper surface and the axis aligned as depicted in Fig. 2(b). (a,e,i,m) Extended [Hz]/[Ho] maps of modes A, B, C, D divided in first (I) and second (II) order modes; (b,f,j,n) detail of the [Hz]/[Ho] maps, two periods of the grating are visible on the upper surface; (c,g,k,o) and (d,h,l,p) detail maps of the electric field components along the y and x axis. GM+ and GM- distinction refers to higher wavelength (A, C) and lower wavelength (B, D) modes among the peak pairs, as resulting from Eq. (1).

within 100 - 150 nm out of the guide; this is promising in view of nanofluidic refractive index sensing applications.

In order to tune the waveguided modes within a broader spectrum, we investigate the optical response of nanopatterns formed by nanostripes of identical cross section and different periodicity (Fig. 1(c), 1(d), 1(e), 1(f). Fig. 4 compares the detected microspectra with calculated responses of four different samples with increasing periodicity. Figure panels are sorted by increasing the pattern periodicity from top (P = 700 nm - Fig. 4(a) to bottom (P = 1300 nm - Fig. 4(j), while the side panels (Fig. 4(b), 4(e), 4(h), 4(k) show the corresponding simulated response. As previously noticed, every pattern is characterized by interband transition in Au below 500 nm wavelength, and by multiple absorption minima in the red-shifted part of the spectrum. For TM polarization, a broadband mode is clearly detected at about 700 nm wavelength, corresponding to the plasmonic lattice resonance. The spectral position of this mode is kept constant in the different arrays provided the fixed aspect ratio of the nanostripes. However, the broadband plasmonic mode is resonantly coupled to guided modes at detuned frequencies depending on the grating periodicity. Conversely, the guided modes excited in sample P700 at 900 nm and 940 nm respectively (Fig. 4(a), display a different behaviour: a gradual red-shift is detected as the grating periodicity increases. In particular, for $P = 900$ nm, the modes red-shift to about 1050 nm and 1090 nm as shown in the VIS-NIR experimental spectra of Fig. 4(d) and labeled as first order (I) in the simulations of Fig. 4(e) and Fig. 4(f).

Fig. 4(c), 4(f), 4(i), 4(l) correspond to simulated spectra within the NIR range (1000-1500 nm) and allow us to follow the spectral position of the first order modes for the higher periodicity samples outside the experimentally observable range. The first order guided modes detected for

Optics EXPRESS

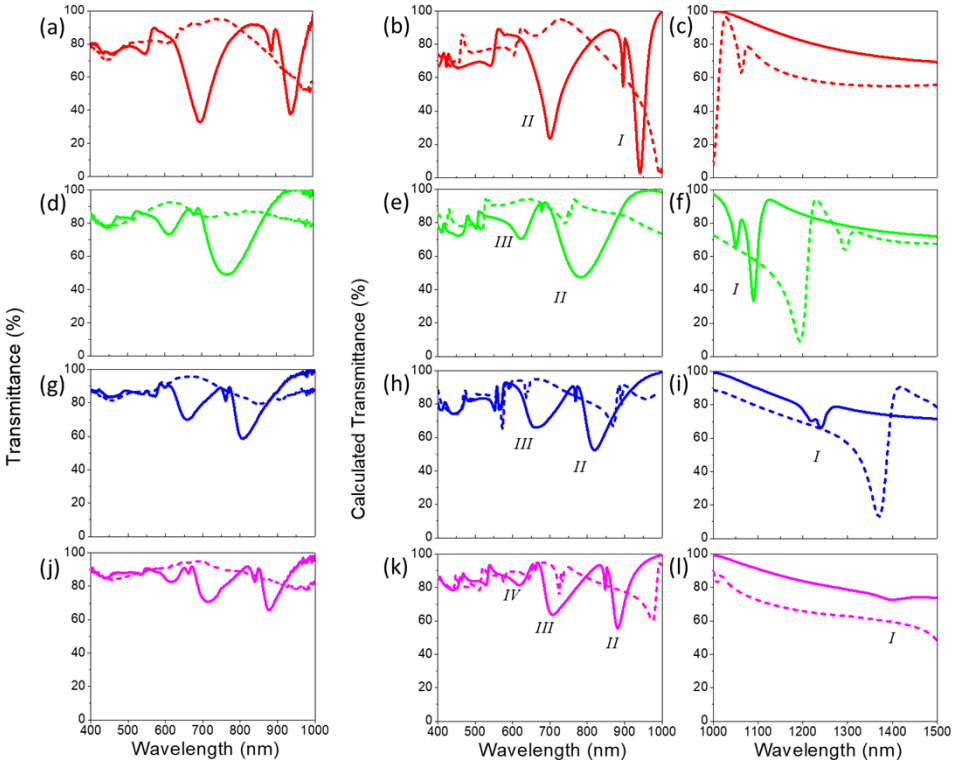

Fig. 4. Spectral shift of the modes obtained by variation of the grating periodicity, P = (a) 700, (d) 900, (g) 1100, (j) 1300 nm. (a,d,g,j) experimental spectra of the gratings; (b,e,h,k) calculated spectra of the nanostripes in the experimentally observed spectral range; (c,f,I,l) calculated extended-range spectra in the Near IR. The order of the guided modes is labeled with letters in the simulated spectra.

P700 gradually red-shift as periodicity increases, in parallel the second and third order excitations are detected in sample P900 and P1100 (Fig. 4(d) and 4(g), and the fourth order emerges in sample P1300 (Fig. 4(j).

Observing the stitched full-range simulated curves (the two columns on the right in Fig. 4), up to four pairs of modes can be recognized for the patterns with larger periodicity. Array P1300 exhibits its first order guided modes (I) at 1400 nm, its second order (II) at 850-900 nm, the third (III) at 650-700 nm, and the fourth (IV) at 550-600 nm.

The second order modes in samples P700 and P900 – or the third order in P1100 and P1300 – are broader with respect to the other modes arising from the same array. When the modes are interacting with the plasmon, indeed, they show an increased intensity of the absorption peaks and relative broadening of the resonance due to the plasmonic dampening. This consideration assumes critical importance in the context of the sensing applications. Indeed, the spectral width of the mode is a key parameter in view of refractive index sensing, limiting the resolution of the spectroscopic detection and the sensitivity of the technique.

Within the set of samples described in this work, the tuning capabilities allowed us to achieve different coupling conditions between the narrowband waveguided modes and the lattice resonance. This is highlighted by the different shapes of the resonance detected at about 700 nm wavelength in all the samples, and confirmed by corresponding calculation of both spectra and near-field distribution. Among the observed responses, P1100 displays high intensity and

Optics EXPRESS

narrowband second-order waveguided modes excitation at about 800 nm wavelength (Fig. 4(g). As confirmed by calculation of the spectra (Fig. 4(h) and the near-field distribution (Supporting Content - Fig. S3 in Supplement 1), the second-order waveguided modes are here detuned from the plasmonic resonance and show a dominant waveguided behaviour. In particular, we would like to exploit its characteristic electric field amplification within a broader liquid volume for refractive index sensing, as shown by the Ey/E0 map of Fig. S3(g) in Supplement 1.

To test the performance of this flat-optics system, we devised a proof-of-concept experiment based on the free-standing plasmonic/photonic templates operating as nanofluidic refractive index sensors. To get quantitative information, the chip has been mounted on a transparent glass support as sketched in Fig. 5(a). The fluidic microchannel enables controlled confinement of sub-picoliter volumes of liquid in the active area. This configuration enables direct in-situ optical detection of transmission micro-spectra under normal incidence illumination (as shown in Fig. 2(a). Different liquids with known refractive index (water, iso-propanol, PMMA/ethyl-lactate solution) have been dosed in contact with the upper, structured side of the membrane, monitoring the spectral shift of the optical modes.

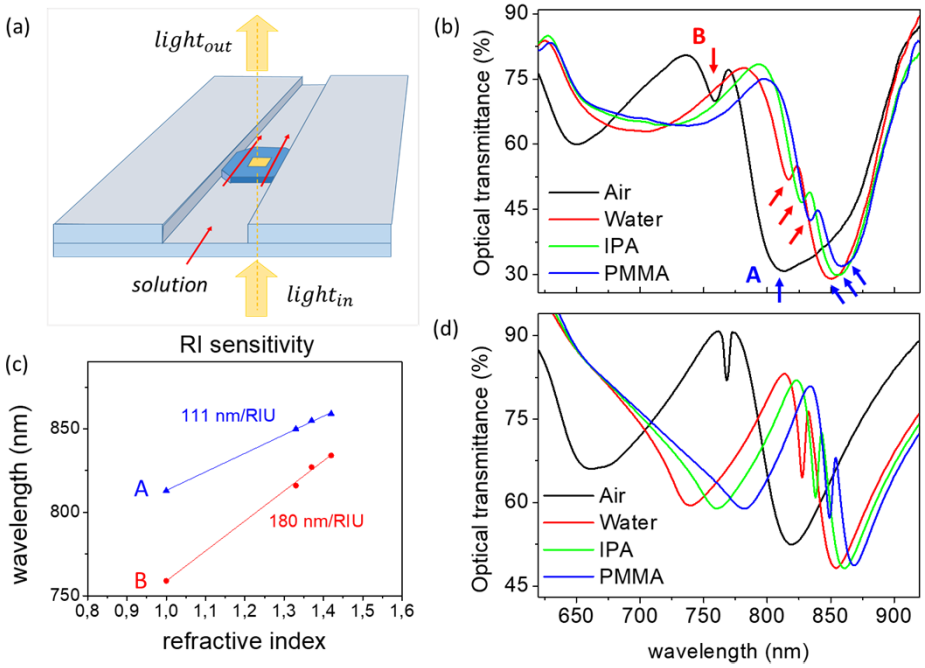

Fig. 5. Testing of the device sensing capability. (a) Sketch of the measure configuration: the active area is highlighted in yellow, the red arrows indicate the flow of tested solution inside the channel; (b) in-situ spectra of the sample, liquids from top to bottom with increasing refractive index; (c) plotted spectral position of the peaks A and B in air (n = 1), water (n = 1.33), IPA (n = 1.37) and PMMA solution (n = 1.42), with estimated Refractive Index sensitivity obtained fitting the spectral shifts (nm/RIU); (d) simulation of the spectral shift with the attributed refractive indices.

Fig. 5(b) compares the VIS-NIR transmittance micro-spectra detected when the active area of P1100 nanograting samples different dielectric environments: air (black curve), water (red curve), iso-propanol (IPA) (green curve) and a PMMA-ethyl-lactate solution (blue curve). A gradual redshift of all the optical modes is detected as the refractive index increases from air- (n = 1) to PMMA- environment (n = 1.42). In order to evaluate the spectral sensitivity of this template we selected the narrowband second-order guided modes (see Fig. 4(h), resonant in air at

Optics EXPRESS

770 nm (mode B) and 810 nm (mode A), and characterized by optimal bandwidth. A red-shift of more than 50 nm has been detected for both the targeted peaks as n increases from 1 to 1.42. In parallel, the resonant frequency of these modes linearly depends on the refractive index, as highlighted by the plot of Fig. 5(c), and further confirmed by data fit. The latter allows the evaluation of the refractive index sensitivity ($\Delta\lambda/\Delta n$), corresponding to the slope of the curve and reading 180 nm/RIU for mode B (red arrow in Fig. 5(b), and 110 nm /RIU for mode A (blue arrow in Fig. 5(b).

The corresponding simulated spectra of this nanosensor (Fig. 5(d), well matched with the experimental data (Fig. 5(b), further confirming the good optical sensitivity of this platform based on guided photonic modes. In particular, the mode B (as seen for P700 in Fig. 3(g), is characterized by minimal bandwidth and by strong near-field confinement at the external interface of the metasurface, thanks to the resonant hot-spots, and represents a good candidate for more complex nanofluidic sensing platforms enabling detection of weak molecular signals. Depending on the desired sensing application and the adopted detection scheme, gratings with different aspect ratio and/or periodicity can be fabricated to evaluate different coupling conditions between the guided modes and the plasmonic response. For example we show in Fig. S4 in Supplement 1 optimized parameters for enhanced refractive index sensitivity up to 600 nm/RIU. On the other hand, if sharp resonances are required, the simulated spectra of Fig. 5(d) suggests that the spectral width of the waveguided mode could be reduced down to 5 nm in an optimized sample, with possible improvement of the refractive index sensing performances [54]. Finally, a study of the field's hot spots, (like the ones in Fig. 3 and in Fig. S3 in Supplement 1) could be performed to enhance light-matter interaction aiming at the detection of single molecules.

Another interesting pathway to increase the sensing capability of the device involves reduction of the minimum sampled volume. By simply designing a fluidic channel with drastically reduced gap in the ten micrometers range, the sensed volume can be downscaled to the picoliter scale. As a lower limit at the molecular scale one can consider examples of nanofluidic applications in which the grating itself is exploited as a channel spacer which sustains a 2D material flake acting as the ceiling of a nanometer size channel [47].

3. Conclusions

Flat-optics nanosensor templates based on plasmonic gratings have been fabricated via high resolution electron beam lithography at the surface of free-standing silicon nitride (Si_3N_4) membranes. These engineered templates are able to host both a broadband plasmonic lattice resonance and different narrowband optical modes launched by the nanograting into the waveguide. A qualitative and semi-quantitative agreement has been achieved between measured optical microspectra and simulations, demonstrating the capability to tune narrowband waveguided modes over a wide VIS-NIR spectral range by simply tailoring the periodicity of the lattice. The optimal bandwidth of these photonic modes, as low as 12 nm, combined with their strong near-field confinement at the external interface, enable the development of a hybrid photonic/plasmonic free-standing nanofluidic device. A proof-of-concept refractive index sensing experiment, at the sub-picoliter scale, showed a good refractive index sensitivity of 180 nm/RIU, for this free-standing platform, enabled by the narrowband waveguided mode (mode B), in optimal agreement with simulations. The latter suggest a further improvement of the refractive index sensitivity in nanoarrays where bandwidth as low as 5 nm can be achieved. The high sensitivity provided by waveguided modes thus suggests these free-standing flat-optics platforms as optimal candidates for label-free biosensing into nanofluidic systems, diagnostics, and environmental detection.

Optics EXPRESS

4. Experimental methods

Silicon nitride membranes by Agar Scientific (Fig. S1(a) and S1(b) in Supplement 1) are applied as functionalized substrates, with free-standing thickness of 200 nm and lateral window size of 500 µm. The thin membrane is supported by a 200 µm -thick silicon wafer which grants mechanical stability and allows safe handling of the chip, with a selectively etched aperture below the free-standing window.

Nanostructures fabrication is performed in a Hitachi SU3500 electron microscope equipped with a Raith lithography module (ELPHY Quantum) using a 30 kV electron beam on a 160 nm thick PMMA film from All Resist (AR-P 690.3), spin coated on the sample surface at 4 krpm and thermally treated (150 °C, 3 min). Development is applied in MIBK-IPA 1:3 solution and then gold is deposited at normal incidence through the mask via calibrated physical vapour deposition in ultra-high vacuum. The thickness of the metallic layer is monitored in-situ with a calibrated quartz crystal microbalance. Lift-off of the polymer mask is then conducted with overnight treatment in stirred acetone, using a magnetic stirrer and a custom support to hold the sample above it.

Optical characterization is conducted with a custom microspectrometer consisting in a Labomed optical microscope (Lx400 trinocular) fibre-coupled to a Vis-NIR high-resolution solid-state spectrometer (HR4000, Ocean Optics), with the blue-light filter and the iris diaphragm originally mounted below the sample replaced by a rotating polarizer (Glan-Thompson). The reduced spot diameter is granted by the core dimension of the collecting optical fibre, attached to the top of the microscope in place of a Labomed digital camera.

Numerical simulations are performed by using Ansys Lumerical FDTD software. In order to take into account the finite size of both the incident beam and the device, periodic boundary conditions cannot be applied. Thus the input field is modeled as a focused Gaussian beam of 10 µm waist impinging on a 50 µm long GMR grating. This condition allows for an optimal trade-off between required computing resources and reliability of the numerical calculation with respect to the real setup.

RI sensing experiments are conducted attaching the sample with a thermal mounting wax (TED Pella Quickstick 135) in a fluidic channel (see Fig. 5(a) made up of optical microscopy glass slabs and closed by a thin glass coverslip. Liquids of known refractive index are then injected in the canal using a syringe, varying the refractive index of the surrounding medium (water, IPA, PMMA solution = 1.33, 1.37, 1.42). The probed volume is limited by the light spot diameter (~20 µm) and the vertical gap between the nanostructures and the glass coverslip (~150 µm), leading to a value of about ten picoliters. Such volume can be easily reduced at sub-picoliter levels by choosing the vertical gap ~15 µm.

Funding. Ministero dell'Istruzione, dell'Università e della Ricerca (Dipartimento di Eccellenza 2018-2022); Regione Liguria (Programma Operativo Regione Liguria FSE 2014-2020); FP7 International Cooperation (Italia- Vietnam, Progetti di Grande Rilevanza 2021 -2023, project H2D).

Acknowledgments. F. Buatier de Mongeot and M. C. Giordano acknowledge financial support by Ministero dell'Università e della Ricerca, within the project 'Dipartimento di Eccellenza 2018-2022' art. 1, c. 314-337, Legge 232/2016. F. Buatier de Mongeot, G. Manzato and D. Chowdhury acknowledge financial support by Regione Liguria within the project 'Programma Operativo Regione Liguria FSE 2014-2020'. M. C. Giordano acknowledges financial support by Ministero degli Affari Esteri e della Cooperazione Internazionale within the bilateral project Italy-Vietnam 2021-2023 'Large-area 2D/plasmonic heterostructures for photocatalysis and energy storage (H2D)'.

Disclosures. The authors declare no conflicts of interest.

Data availability. Data underlying the results presented in this paper are not publicly available at this time but may be obtained from the authors upon reasonable request.

Supplemental document. See Supplement 1 for supporting content.

Optics EXPRESS

References

1. H. Zhang, B. Abhiraman, Q. Zhang, J. Miao, K. Jo, S. Roccasecca, M. W. Knight, A. R. Davoyan, and D. Jariwala, "Hybrid Exciton-Plasmon-Polaritons in van Der Waals Semiconductor Gratings," Nat. Commun. **11**(1), 3552 (2020)..
2. S. Baur, S. Sanders, and A. Manjavacas, "Hybridization of Lattice Resonances," ACS Nano **12**(2), 1618–1629 (2018)..
3. M. Barelli, A. Mazzanti, M. C. Giordano, G. Della Valle, and F. Buatier de Mongeot, "Color Routing via Cross-Polarized Detuned Plasmonic Nanoantennas in Large-Area Metasurfaces," Nano Lett. **20**(6), 4121–4128 (2020)..
4. A. Camposeo, L. Persano, M. Farsari, and D. Pisignano, "Additive Manufacturing: Applications and Directions in Photonics and Optoelectronics," Advanced Optical Materials **7**(1), 1800419 (2019)..
5. J. Zhang, J. Yang, H. Xin, J. Huang, D. Chen, and Z. Zhaojian, "Ultrashort and Efficient Adiabatic Waveguide Taper Based on Thin Flat Focusing Lenses," Opt. Express **25**(17), 19894 (2017)..
6. A. A. Yanik, M. Huang, A. Artar, T.-Y. Chang, and H. Altug, "Integrated Nanoplasmonic-Nanofluidic Biosensors with Targeted Delivery of Analytes," Appl. Phys. Lett. **96**(2), 021101 (2010)..
7. A. F. Coskun, A. E. Cetin, B. C. Galarreta, D. A. Alvarez, H. Altug, and A. Ozcan, "Lensfree Optofluidic Plasmonic Sensor for Real-Time and Label-Free Monitoring of Molecular Binding Events over a Wide Field-of-View," Sci. Rep. **4**(1), 6789 (2015)..
8. Y. Li, C. Chen, K. Willems, S. Kerman, L. Lagae, G. Groeseneken, T. Stakenborg, and P. Van Dorpe, "Probing Local Potentials inside Metallic Nanopores with SERS and Bipolar Electrochemistry," Advanced Optical Materials **5**(15), 1600907 (2017)..
9. D. Rodrigo, A. Tittl, A. John-Herpin, O. Limaj, and H. Altug, "Self-Similar Multiresonant Nanoantenna Arrays for Sensing from Near- to Mid-Infrared," ACS Photonics **5**(12), 4903–4911 (2018)..
10. Md S. Islam, J. Sultana, R. Ahmmed Aoni, Md S. Habib, A. Dinovitser, B. W.-H. Ng, and D. Abbott, "Localized Surface Plasmon Resonance Biosensor: An Improved Technique for SERS Response Intensification," Opt. Lett. **44**(5), 1134 (2019)..
11. L. M. S. Aas, M. Kildemo, C. Martella, M. C. Giordano, D. Chiappe, and F Buatier de Mongeot, "Optical Properties of Biaxial Nanopatterned Gold Plasmonic Nanowired Grid Polarizer," Opt. Express **21**(25), 30918 (2013)..
12. Z. Liao, Y. Zhang, Y. Li, Y. Miao, S. Gao, F. Lin, Y. Deng, and L. Geng, "Microfluidic Chip Coupled with Optical Biosensors for Simultaneous Detection of Multiple Analytes: A Review," Biosens. Bioelectron. **126**, 697–706 (2019)..
13. D.-S. Wang and S.-K. Fan, "Microfluidic Surface Plasmon Resonance Sensors: From Principles to Point-of-Care Applications," Sensors **16**(8), 1175 (2016)..
14. A. Belardini, A. Benedetti, M. Centini, G. Leahu, F. Mura, S. Sennato, C. Sibilia, V. Robbiano, M. C. Giordano, C. Martella, D. Comoretto, and F. B. de Mongeot, "Second Harmonic Generation Circular Dichroism from Self-Ordered Hybrid Plasmonic-Photonic Nanosurfaces," Advanced Optical Materials **2**(3), 208–213 (2014)..
15. S. S. Aćimović, M. A. Ortega, V. Sanz, J. Berthelot, J. L. Garcia-Cordero, J. Renger, S. J. Maerkl, M. P. Kreuzer, and R. Quidant, "LSPR Chip for Parallel, Rapid, and Sensitive Detection of Cancer Markers in Serum," Nano Lett. **14**(5), 2636–2641 (2014)..
16. D. V. Verschueren, S. Pud, X. Shi, L. De Angelis, L. Kuipers, and C. Dekker, "Label-Free Optical Detection of DNA Translocations through Plasmonic Nanopores," ACS Nano **13**(1), 61–70 (2019)..
17. X. Shi, D. V. Verschueren, and C. Dekker, "Active Delivery of Single DNA Molecules into a Plasmonic Nanopore for Label-Free Optical Sensing," Nano Lett. **18**(12), 8003–8010 (2018)..
18. Q. Yang, M. Liu, S. Kruk, Y. Xu, Y. K. Srivastava, R. Singh, J. Han, Y. Kivshar, and I. V. Shadrivov, "Polarization-Sensitive Dielectric Membrane Metasurfaces," Adv. Opt. Mater. **8**(20), 2000555 (2020)..
19. A. Siria, M.-L. Bocquet, and L. Bocquet, "New Avenues for the Large-Scale Harvesting of Blue Energy," Nat. Rev. Chem. **1**(11), 0091 (2017)..
20. I. I. Hosseini, Z. Liu, X. Capaldi, T. AbdelFatah, L. Montermini, J. Rak, W. Reisner, and S. Mahshid, "Nanofluidics for Simultaneous Size and Charge Profiling of Extracellular Vesicles," Nano Lett. **21**(12), 4895–4902 (2021)..
21. A. Leitis, M. L. Tseng, A. John-Herpin, Y. S. Kivshar, and H Altug, "Wafer-Scale Functional Metasurfaces for Mid-Infrared Photonics and Biosensing," Adv. Mater. **33**(43), 2102232 (2021)..
22. M. P. Jonsson, A. B. Dahlin, L. Feuz, S. Petronis, and F. Höök, "Locally Functionalized Short-Range Ordered Nanoplasmonic Pores for Bioanalytical Sensing," Anal. Chem. **82**(5), 2087–2094 (2010)..
23. C. Novara, A. Lamberti, A. Chiadò, A. Virga, P. Rivolo, F. Geobaldo, and F. Giorgis, "Surface-Enhanced Raman Spectroscopy on Porous Silicon Membranes Decorated with Ag Nanoparticles Integrated in Elastomeric Microfluidic Chips," RSC Adv. **6**(26), 21865–21870 (2016)..
24. E. S. Prikhozhdenko, D. N. Bratashov, D. A. Gorin, and A. M. Yashchenok, "Flexible Surface-Enhanced Raman Scattering-Active Substrates Based on Nanofibrous Membranes," Nano Res. **11**(9), 4468–4488 (2018)..
25. M. C. Giordano, M. Tzschoppe, M. Barelli, J. Vogt, C. Huck, F. Canepa, A. Pucci, and F. Buatier de Mongeot, "Self-Organized Nanorod Arrays for Large-Area Surface-Enhanced Infrared Absorption," ACS Appl. Mater. Interfaces **12**(9), 11155–11162 (2020)..
26. D. Repetto, M. C. Giordano, A. Foti, P. G. Gucciardi, C. Mennucci, and F. Buatier de Mongeot, "SERS Amplification by Ultra-Dense Plasmonic Arrays on Self-Organized PDMS Templates," Appl. Surf. Sci. **446**, 83–91 (2018)..

Optics EXPRESS

27. M. Barelli, M. C. Giordano, P. G. Gucciardi, and F. Buatier de Mongeot, "Self-Organized Nanogratings for Large-Area Surface Plasmon Polariton Excitation and Surface-Enhanced Raman Spectroscopy Sensing," ACS Appl. Nano Mater. **3**(9), 8784–8793 (2020)..
28. L. Sarcina, E. Macchia, G. Loconsole, G. D'Attoma, P. Saldarelli, V. Elicio, G. Palazzo, and L. Torsi, "Surface Plasmon Resonance Assay for Label-Free and Selective Detection of *Xylella Fastidiosa*," Adv NanoBio Res **1**(10), 2100043 (2021)..
29. A. M. Shrivastav, U. Cvelbar, and I. Abdulhalim, "A Comprehensive Review on Plasmonic-Based Biosensors Used in Viral Diagnostics," Commun. Biol. **4**(1), 70 (2021)..
30. B. Fazio, C. D'Andrea, F. Bonaccorso, A. Irrera, G. Calogero, C. Vasi, P. G. Gucciardi, M. Allegrini, A. Toma, D. Chiappe, C. Martella, and F. Buatier de Mongeot, "Re-Radiation Enhancement in Polarized Surface-Enhanced Resonant Raman Scattering of Randomly Oriented Molecules on Self-Organized Gold Nanowires," ACS Nano **5**(7), 5945–5956 (2011)..
31. S.-G. Park, C. Mun, X. Xiao, A. Braun, S. Kim, V. Giannini, S. A. Maier, and D.-H. Kim, "Surface Energy-Controlled SERS Substrates for Molecular Concentration at Plasmonic Nanogaps," Adv. Funct. Mater. **27**(41), 1703376 (2017)..
32. U. Fano, "Effects of Configuration Interaction on Intensities and Phase Shifts," Phys. Rev. **124**(6), 1866–1878 (1961)..
33. Y. Francescato, V. Giannini, and S. A. Maier, "Plasmonic Systems Unveiled by Fano Resonances," ACS Nano **6**(2), 1830–1838 (2012)..
34. D. Chowdhury, M. C. Giordano, G. Manzato, R. Chittofrati, C. Mennucci, and F. Buatier de Mongeot, "Large-Area Microfluidic Sensors Based on Flat-Optics Au Nanostripe Metasurfaces," J. Phys. Chem. C **124**(31), 17183–17190 (2020)..
35. J. Liu, Z. Liu, and H. Hu, "Tunable Multiple Fano Resonance Employing Polarization-Selective Excitation of Coupled Surface-Mode and Nanoslit Antenna Resonance in Plasmonic Nanostructures," Sci. Rep. **9**(1), 2414 (2019)..
36. T. Cao and L. Zhang, "Enhancement of Fano Resonance in Metal/Dielectric/Metal Metamaterials at Optical Regime," Opt. Express **21**(16), 19228 (2013)..
37. S. Wu, Y. Shen, and C. Jin, "Surface-Enhanced Raman Scattering Induced by the Coupling of the Guided Mode with Localized Surface Plasmon Resonances," Nanoscale **11**(30), 14164–14173 (2019)..
38. M. Bhatnagar, M. Gardella, M. C. Giordano, D. Chowdhury, C. Mennucci, A. Mazzanti, G. D. Valle, C. Martella, P. Tummala, A. Lamperti, A. Molle, and F. Buatier de Mongeot, "Broadband and Tunable Light Harvesting in Nanorippled MoS_2 Ultrathin Films," ACS Appl. Mater. Interfaces **13**(11), 13508–13516 (2021)..
39. M. Bhatnagar, M. C. Giordano, C. Mennucci, D. Chowdhury, A. Mazzanti, G. Della Valle, C. Martella, P. Tummala, A. Lamperti, A. Molle, and F. Buatier de Mongeot, "Ultra-Broadband Photon Harvesting in Large-Area Few-Layer MoS_2 Nanostripe Gratings," Nanoscale **12**(48), 24385–24393 (2020)..
40. H. Jiang, S. Choudhury, Z. A. Kudyshev, D. Wang, L. J. Prokopeva, P. Xiao, Y. Jiang, and A. V. Kildishev, "Enhancing Sensitivity to Ambient Refractive Index with Tunable Few-Layer Graphene/HBN Nanoribbons," Photonics Res. **7**(7), 815 (2019)..
41. J. B. Lassiter, F. McGuire, J. J. Mock, C. Ciracì, R. T. Hill, B. J. Wiley, A. Chilkoti, and D. R. Smith, "Plasmonic Waveguide Modes of Film-Coupled Metallic Nanocubes," Nano Lett. **13**(12), 5866–5872 (2013)..
42. M. Khorasaninejad and F. Capasso, "Broadband Multifunctional Efficient Meta-Gratings Based on Dielectric Waveguide Phase Shifters," Nano Lett. **15**(10), 6709–6715 (2015)..
43. G. Quaranta, G. Basset, O. J. F. Martin, and B. Gallinet, "Recent Advances in Resonant Waveguide Gratings," Laser & Photonics Reviews **12**(9), 1800017 (2018)..
44. S. Joseph, S. Sarkar, and J. Joseph, "Grating-Coupled Surface Plasmon-Polariton Sensing at a Flat Metal–Analyte Interface in a Hybrid-Configuration," ACS Appl. Mater. Interfaces **12**(41), 46519–46529 (2020)..
45. S. Butun and K. Aydin, "Asymmetric Light Absorption and Reflection in Freestanding Nanostructured Metallic Membranes," ACS Photonics **2**(12), 1652–1657 (2015)..
46. E. Sakat, G. Vincent, P. Ghenuche, N. Bardou, S. Collin, F. Pardo, J.-L. Pelouard, and R. Haïdar, "Guided Mode Resonance in Subwavelength Metallodielectric Free-Standing Grating for Bandpass Filtering," Opt. Lett. **36**(16), 3054 (2011)..
47. MT. outerde, A. Keerthi, A. R. Poggioli, S. A. Dar, A. Siria, A. K. Geim, L. Bocquet, and B Radha, "Molecular Streaming and Its Voltage Control in Ångström-Scale Channels," Nature **567**(7746), 87–90 (2019)..
48. S. Kumar, S. Cherukulappurath, T. W. Johnson, and S.-H. Oh, "Millimeter-Sized Suspended Plasmonic Nanohole Arrays for Surface-Tension-Driven Flow-Through SERS," Chem. Mater. **26**(22), 6523–6530 (2014)..
49. V. Giannini, G. Vecchi, and J. Gómez Rivas, "Lighting Up Multipolar Surface Plasmon Polaritons by Collective Resonances in Arrays of Nanoantennas," Phys. Rev. Lett. **105**(26), 266801 (2010)..
50. S. Tuccio, M. Centini, A. Benedetti, and C. Sibilia, "Subwavelength Coherent Control and Coupling of Light in Plasmonic Nanoresonators on Dielectric Waveguides," J. Opt. Soc. Am. B **30**(2), 450 (2013)..
51. C. Tan, J. Simonen, and T. Niemi, "Hybrid Waveguide-Surface Plasmon Polariton Modes in a Guided-Mode Resonance Grating," Opt. Commun. **285**(21-22), 4381–4386 (2012)..
52. J. Zhang, L. Cai, W. Bai, and G. Song, "Hybrid Waveguide-Plasmon Resonances in Gold Pillar Arrays on Top of a Dielectric Waveguide," Opt. Lett. **35**(20), 3408 (2010)..
53. T. Zentgraf, S. Zhang, R. F. Oulton, and X. Zhang, "Ultranarrow Coupling-Induced Transparency Bands in Hybrid Plasmonic Systems," Phys. Rev. B **80**(19), 195415 (2009)..
54. X. Lu, G. G. Zheng, and P Zhou, "High Performance Refractive Index Sensor with Stacked Two-Layer Resonant Waveguide Gratings," Results Phys. **12**, 759–765 (2019)..